On the scaling of avaloids and turbulence with the average density approaching the density limit

G. Y. Antar
University of California San Diego, 9500 Gilman Dr., La Jolla, California 92093-0417

G. Counsell and J.-W. Ahn[a)]
EURATOM/UKAEA Fusion Association, Culham Science Centre, Abingdon, Oxfordshire OX14 3DB, United Kingdom

(Received 11 January 2005; accepted 20 May 2005; published online 25 July 2005)

This article is dedicated to the characterization of turbulent transport in the scrape-off layer of the Mega Ampère Spherical Tokamak [A. Sykes *et al.*, Phys. Plasmas **8**, 2101 (2001)] as a function of the average density (n_L). The aim is to answer a renewed interest in this subject since the bursty character of turbulence in the scrape-off layer was shown to be caused by large-scale events with high radial velocity reaching about 1/10th of the sound speed called avaloids [G. Antar *et al.*, Phys. Rev. Lett **87**, 065001 (2001)]. With increasing density, turbulence and transport increase nonlinearly at the midplane while remaining almost unchanged in the target region. Using various and complementary statistical analyses, the existence of a "critical" density, at $n_L/n_G \simeq 0.35$ is emphasized; n_G is the Greenwald density. Both above and below this density, intermittency decreases and avaloids play a decreasing role in the particle radial transport. This is interpreted as caused by the interplay between avaloids and the surrounding turbulent structures which mix them more efficiently with increasing density as the level of the background turbulence increases. The scaling of the different quantities with respect to the normalized density is obtained. It reveals that not only the level of turbulence and transport increase, but also the radial velocity and length scales. This increases the coupling between the hot plasma edge and the cold scrape-off layer that may explain the disruptive instability occurring at high densities. © *2005 American Institute of Physics*. [DOI: 10.1063/1.1953592]

I. INTRODUCTION

In magnetic fusion devices, the fusion power $P_{\mathrm{fus}} = n^2 F(T)$ is strongly dependent on the average density (n), hence, the attempt to increase it; the average plasma temperature is denoted by T and F is some function of T. By doing so, toroidal fusion devices reported the existence of a density limit above which a major disruption occurs. Under constant edge safety factor, the empirical analysis of the data by Murakami *et al.* led to the conclusion that the density limit scales like B_T/R, where B_T is the toroidal magnetic field and R is the major radius.[1] Later, when a scaling with respect to the plasma current I_p was performed as shown in Ref. 2, a new empirical scaling formula, often called the Hugill scaling, was obtained. It reads

$$n_{\mathrm{lim}} = C_{\mathrm{Hugill}} \frac{I_p}{\pi a^2 g},$$

where a is the minor radius, g characterizes the plasma shape and C_{Hugill} is a constant. A re-examination of the scaling led Greenwald *et al.*[3] to deduce that the density limit does not depend on power and it can be described by the simple relation

$$n_G[\mathrm{m}^{-3}] = 1 \times 10^{20} \frac{I_p[\mathrm{MA}]}{\pi a^2[\mathrm{m}^2]}.$$

This limit was investigated by a large number of toroidal confinement devices;[4–9] for a comprehensive and recent review on the density limit topic, please see Ref. 10. From the various experimental data, it was concluded that the density limit, and unlike the other operational limits, would seem to evolve physics related to the edge and scrape-off layer (SOL) where transport is high.

The role of the edge was recognized early where its cooling would lead to radiative collapse of the plasma in the form of a major disruption.[1] However, nonradiative collapse was also reported in Ref. 2 suggesting other mechanisms such as particle and heat transport (see Ref. 3). This has initiated a large number of experimental (see, for example, Refs. 11–13) as well as theoretical investigations as described in Refs. 14–18. These studies highlighted the role of transport in the main plasma as a major contributor in setting the density limit in tokamaks.

Because the role of the main chamber recycling cannot be neglected and may actually dominate in some cases, the focus turned to the properties of transport in the SOL.[19] In the Joint European Torus (JET), using the density and temperature profiles, the SOL decay length was used to investigate its dependence on the plasma current and density.[20] It was found that roughly $\lambda_n \sim 1/I_p$ and $\lambda_T \sim n/I_p$. In the Alcator C-MOD tokamak, the crucial role of the cross-field par-

[a)]Present address: College of Letters and Science, University of Wisconsin, 1150 Univ. Av., Madison WI 53706.

ticle transport was highlighted as a competing mechanism to the parallel transport to the divertor.[21] The so-called effective diffusion coefficient ($D_{\mathrm{eff}}=-\Gamma_r/\nabla_r n$) is found to increase with the distance to the last closed flux surface (LCFS) increasing the role of cross-field heat conduction as well as charge exchange; D_{eff} was determined at the midplane and Γ_r is the radial turbulent flux. By varying the plasma parameters, it was found that $D_{\mathrm{eff}}\sim T^{-3.5}n^{1.7}$. In Refs. 22 and 23 a detailed investigation of the profiles in the SOL as a function of the average density was made. Depending on the average plasma density, the midplane SOL profile may exhibit one- or two-layer structures. As the average density is increased, the density profile in the region between the LCFS and the wall are flattened while that of temperature remains almost unchanged.

Intermittency in the SOL was reported in nearly all the tokamaks (see, for example, Refs. 24–27). In an effort to characterize its role in the behavior of the profile on C-MOD as the density is increased, the so-called "R/S method" was applied to the data.[28] The Hurst parameter as well as the intermittency coefficient increased with the average density. This was interpreted as suggesting an increasing role of bursty transport. On the other hand, the nature of the intermittent transport was revisited by a series of articles.[29–32] It was shown that the intermittent structures are convective in nature, with a high radial velocity that can reach about 1/10th of the sound speed. Avaloids were thus defined as large-scale coherent concentration of plasma that are encountered intermittently in the SOL having high radial velocities. It was also shown that, even though they may occupy less than 20% of the total duration of a signal, they account for about 50% of the radial transport near the last closed flux surface. Moreover, a direct comparison, using up to eight different statistical analyses, in four different magnetic devices, that are, the MAST, Alcator C-MOD and Tore Supra tokamaks and the plasma linear devices PISCES was performed in Ref. 31. It was emphasized the universal character of avaloids in the sense that they have the same statistical properties in the four devices. More recently, the nature of avaloids was investigated.[32] It was shown that avaloids in PISCES are actually emitted in a more or less periodic and not intermittent fashion and that they result from a saturation of an instability occurring at the plasma edge. However, in tokamaks, the relationship between avaloids and magnetohydromagnetic modes is still to be investigated.

Having on one hand, the results of the Alcator C-MOD tokamak about the flattening of the density profile, and on the other the convective nature of avaloids, it seems natural and rather important to investigate the relationship between turbulence in the SOL and the average density. This is the main topic of this article. Moreover, avaloids existence and universality were shown on different devices at various plasma currents, densities and toroidal magnetic strengths. The second goal that we aim at achieving in this article is to provide the scaling of avaloids properties with respect to average density. It should be regarded as a first step in order to assess how long a future confinement device such as ITER[33] can be operated in L-mode regime taking into account that avaloids lead to hot and dense plasma far from the LCFS.

In order to achieve our goals, we use data taken on MAST.[34–36] Mainly probe data at the midplane and at the divertor target plates are used. The rest of the article continues as follows. Next, the experimental setup of MAST is presented along with the description of the plasma discharges. Then, we show that the average values of the ion saturation current density increase with the average density along with the turbulent fluctuations and the average turbulent radial transport. In Sec. IV, the probability distribution function is analyzed using the third and fourth order moments to characterize intermittency. It is shown that the flatness and the skewness factors both tend to Gaussian values as density is increased. In Secs. V and VI, we turn to analyzing the auto- and cross-correlation properties. The analyses lead us to deduce that small scales are damped. However, fewer large scale structures are present as the cross-correlation amplitude decreases with increasing density. Complementary to the two sections discussing the probability distribution and correlation, Sec. VII analyzes the high amplitude bursts of the signals after using conditional analysis that separates the high from the low intensity bursts. We show that avaloids frequency remains unchanged and thus their contribution to the overall transport decreases for large values of the average density as they interact with the background turbulence. A conclusion follows where we suggest a link between the results of this paper and the problem of the density limit in tokamaks, and we show that there exist a "critical" density around which the role of avaloids peak. The usage of the word "critical" here describes that the effect of avaloids peaks at $n_L/n_G\sim 0.35$ and decreases for both higher and lower densities.

II. THE EXPERIMENTAL SETUP

The Mega Ampère Spherical Tokamak (MAST) has an aspect ratio R/a about 1.56 ($R=0.84, a=0.54$) much smaller than conventional tokamaks such as Alcator C-Mod where it is about 3.33. The gas used for our study is deuterium, and the main plasma parameters are: magnetic field 0.6 T and plasma current 0.7 MA. The plasma is in L-mode and Ohmically heated. MAST does not have a first wall close to the plasma which may make the problem of the main chamber recycling less crucial. The reference density (n_L) is given by an interferometer normalized to the Greenwald density, denoted by n_G, as it was defined in the Introduction. Greenwald density limit for the plasma discharges investigated here is 0.85×10^{20} m^{-3}. Lower double null (LDN) and connected double (CDN) null divertor configuration are used.[37] The normalized density on MAST ranges between 0.24 and 0.72 achieved by a low-field gas puffing. Hence, even though the density limit is not attained in this experiment we still believe that the range of the density investigated here is sufficient to draw conclusions about the scaling of the turbulence and the role of convective transport with respect to the average density. The reciprocating probe is located at the outer midplane and contains three sets of tips. Each set contains three tips. The diameter of each tip is 0.15 cm and the po-

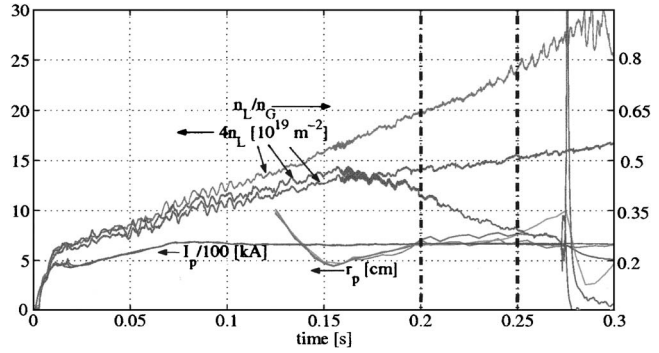

FIG. 1. The line-integrated density for three discharges 6860, 6861, and 6862 as a function of time where the magnetic configuration is CDN. When normalized to the Greenwald density the resultant values are inserted on the right-hand side. The corresponding plasma current is shown and the radial position of the reciprocating midplane probe to the LCFS. The two vertical dash-dotted lines indicate the time range where data are analyzed.

loidal distance among one set of tips is 0.5 cm. In the radial direction the distance between the two set of probes is 0.5 cm. One set of probes used contain one biased to the ion saturation current, and the other two are poloidally separated and floating from which the radial electric field is deduced. The acquisition frequency is 1 MHz. For the data used here, the probe distance to the separatrix is about 7 cm. The probe position was kept fixed during the discharge but the plasma major and minor radii changed leading to the evolution described in Fig. 1 of the probe position to the last closed flux surface. Having to select a time period where the probe position is about 7 cm leads to the fact that not all the discharge is analyzed; hence, hereafter the analyzed data points will appear in clusters. Also are used flush-mounted target probes to study the behavior of the target region with increasing density. They have a circular shape with 0.4 cm diameter; their acquisition frequency is also set to 1 MHz.

In Fig. 1 we plot the line-integrated density for the CDN case where the values of average density range from 0.4 to 0.8×10^{19} m^{-3}. We assume that the temperature does not change much having a value of about 20 eV in the SOL. The electron-electron collision frequency changes from approximately 18.6×10^{6} s^{-1} to 9.32×10^{6} s^{-1}. Taking into account that electrons parallel velocity is that of the sound speed leads to a collisionality in the SOL that goes from 50 to 100. Therefore in all cases plasma in the SOL is considered to be collisional. Also shown is the probe position to the last closed flux surface and the plasma current. Because the probe's distance to the LCFS changes, results from the region that lies between the two vertical dash-dotted lines are reported. The shot numbers for the CDN case are 6860, 6861, and 6862. For the LDN case, they are 6843, 6846, 6847, 6848, and 6849.

III. THE FIRST TWO ORDER MOMENT'S DEPENDENCE ON THE NORMALIZED DENSITY

In this section, the average and the standard deviations of the ion saturation current density ($j_{sat}=nc_s$ where c_s is the sound speed) are used to characterize the far SOL. The full data length is divided into subsets of 20 000 points; this number is determined by the stationary condition imposed for accurate statistical analysis of the data. The first order moment is the average value and is used to assess the dependence of the average density in the SOL as a function of the line-averaged density. Once this is done, the average value is subtracted from the signals and the second order moment is discussed. In this section, the error bars on the exponents determined by fitting the data to power laws are about 10%. Within this value, no difference is found in the SOL behavior in CDN or LDN magnetic configurations. Accordingly, hereafter, data from the two magnetic configurations will be included in the same graph to obtain the scaling with respect to the average density.

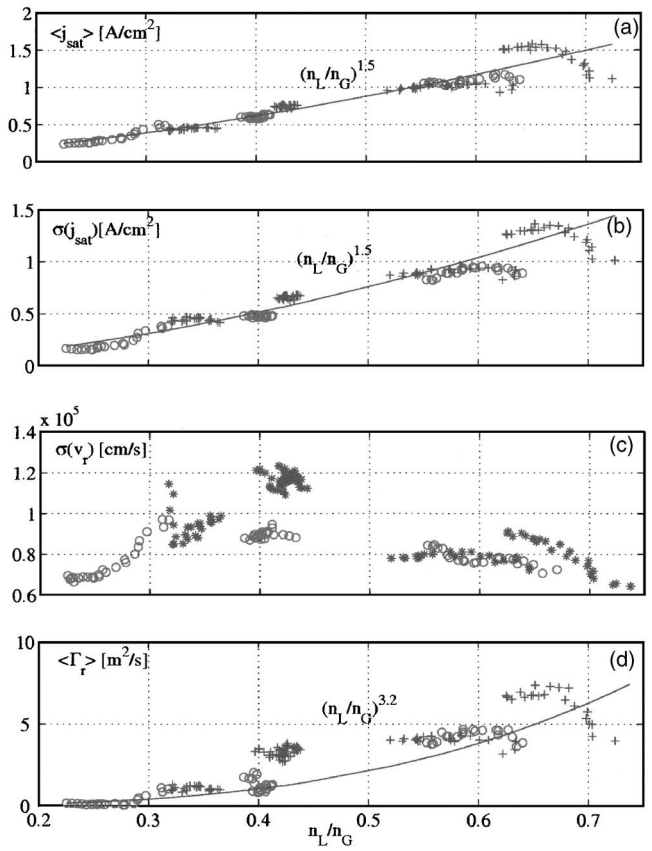

FIG. 2. The average ($\langle j_{sat}\rangle$) and standard deviation ($\sigma(j_{sat})$) of the ion saturation current density are plotted in (a) and (b), respectively. The standard deviation of the radial velocity fluctuations is shown in (c). In (d) the average value of the turbulent radial flux as a function of n_L/n_G is plotted. The best fits are shown in solid lines along with the scaling law obtained. The (○) and (+) denote CDN and LDN magnetic configuration. In (d), the origin of the deviation from the fitting curve at $n_L/n_G\sim0.4$ is not yet understood.

A. The average value of j_{sat}

The first order moment is the average value of a fluctuating quantity. In Fig. 2(a) the average value of the ion saturation current density is plotted. The $\langle\,\rangle$ denotes temporal averaging. It increases with increasing normalized density according to the power law

$$\langle j_{\mathrm{sat}} \rangle \sim (n_L/n_G)^{1.5}.$$

This dependence can be considered as a lower bound for the density in the far SOL since the temperature is recorded to stay almost constant or slightly decrease with increasing n_L/n_G.

In C-MOD, the density and temperature behavior in the SOL has actually been extensively studied by sweeping the probe voltage.[22,23] The temperature profile remained nearly unchanged while that of the density increased with the formation of a plateau that lies between the first wall and the separatrix. Accordingly, one can rather safely assume that the increase of j_{sat} is mainly caused by the density.

B. The standard deviation of j_{sat} and v_r

In Fig. 2(b) the standard deviation representing the level of fluctuations as a function of n_L/n_G is shown. The level of fluctuations increases at the same rate as the average value with respect to the normalized density. This is consistent with the idea that the source of the particle flux in the SOL is turbulent fluctuations where a higher level of turbulence leads to higher densities.

The radial velocity v_r corresponds to the $\vec{E}\times\vec{B}$ drift as it is calculated using the two poloidally separated floating probes. In Fig. 2(c) the behavior of the standard deviation of v_r is plotted. The dependence with the normalized density is not monotonic as is the case of the density fluctuations. $\sigma(v_r)$ increases for normalized densities smaller than 0.4 and it remains unchanged within the experimental error bars for larger values.

C. The average turbulent radial flux

The turbulent radial transport $\Gamma_r = \langle n' v_r' \rangle$ is shown in Fig. 2(d) as a function of the normalized density. The primes represent the fluctuating quantities of the density and the radial velocity obtained after subtracting the average value from the signals. The best fit of the data leads to the power law of the form

$$\Gamma_r \sim (n_L/n_G)^{3.2}.$$

The difference in the power laws of the level of fluctuations and the radial flux can be caused by either the radial velocity fluctuations increase or/and increase of the coupling between the density and radial velocity. As it was shown, $\sigma(v_r)$ remains rather constant. Consequently, the strong dependence of the radial flux on the normalized density is mainly caused by a more efficient coupling between the density and the radial velocity fluctuations. In other words, the phase between density and radial velocity fluctuations tends toward 0 with increasing normalized density.

IV. THE PROBABILITY DISTRIBUTION FUNCTION VS THE NORMALIZED DENSITY

The previous paragraph described the average and standard deviation dependencies on the normalized density. Hereafter, the average value is subtracted from the data series and then we divide by the standard deviation. It was shown by many authors[25,30,31] that the probability distribution functions (PDFs) of the ion saturation current fluctuations are skewed toward positive values. The normalized third and fourth order moments, called the skewness and flatness (or kurtosis) factors, are used to describe the asymmetry and the weight of the distribution tail, respectively. For a Gaussian, they take the values of 0 and 3, but in the SOL, the skewness and the flatness factors were found to be greater than 0 and 3. This deviation was shown to be caused by avaloids as their density and temperature is much higher than the background.[30] The diffusive component of turbulence, on the other hand, has a smaller radial velocity and is thus more affected by the parallel transport. By using the skewness and flatness factors, one is able to quantify avaloids frequency and intensity with respect to the standard deviation. For example, a flatness factor equal to 3, would mean that avaloids are rare and PDF reflecting high intensities decay according to a Gaussian law. The higher the flatness factor is the more important are the avaloids contribution to the overall turbulence. This method using the high order moments of the PDF cannot, however, distinguish between bursts intensity and frequency. High intensity bursts can lead to the same skewness and flatness factors as low intensity bursts but more frequent. Nevertheless, this method is straightforward and provides information about avaloids contribution to turbulence as the normalized density is increased.

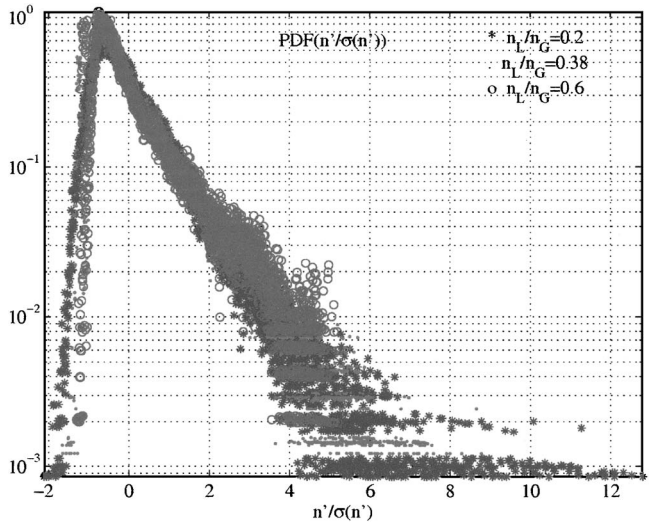

FIG. 3. Three PDFs taken at different normalized densities 0.2 (stars) 0.38 (dots) and 0.6 (circles). The plot is semi-logarithmic and the density fluctuations were normalized by their standard deviation. Note that the tail of the distribution gets shorter with increasing density.

A. The PDF tendency toward Gaussian with increasing normalized density

In Fig. 3 three PDFs taken at different n_L/n_G are shown in a semi-logarithmic plot. First, let us note that because the PDF is skewed toward positive fluctuations, a difference exists between the average value and the most probable value. The latter is estimated as corresponding to the maximum of the PDF; because the average value is set to 0, the most probable value is negative.

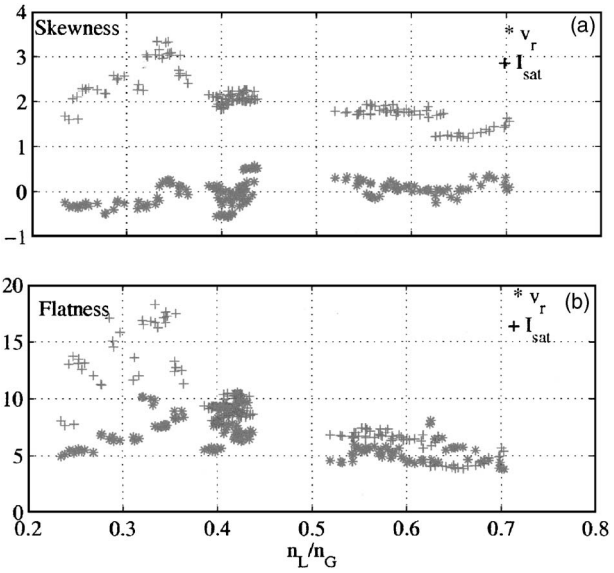

FIG. 4. In (a) and (b) respectively, the skewness and flatness factors are plotted against the normalized density for the density (+) and the radial velocity fluctuations (∗). Note that the skewness and flatness factors of the ion saturation current fluctuations peaks at around n_L/n_G and tend toward Gaussian values for lower and higher values of the density.

On the negative side of the density fluctuations, the sharp decrease of the PDF is indicative of the Gaussian character of the fluctuations as the graph is semi-logarithmic. As n_L/n_G is increased, the positive tail of the distribution is observed to get shorter going from eight to four times the standard deviation. This is a clear indication that the intermittent bursts are getting smaller in amplitude with respect to the overall standard deviation of the signal.

B. Confirming using the skewness and flatness factors

The skewness and the flatness factors of the ion saturation current and the radial velocity are plotted in Fig. 4. We recall that data are taken in Ohmically heated L-mode discharges under two magnetic configurations that are LDN and CDN.

Figure 4(a) shows the skewness factor of the ion saturation current. It increases with the normalized density for $n_L/n_G<0.35$ going from 1.5 to 3. For $n_L/n_G>0.35$ the skewness factors monotonously decreases from 3 to approximately 1. The PDF asymmetry of the radial velocity fluctuations seems, on the other hand, to be little affected by the increase of the normalized density.

The flatness factor of the ion saturation current density behaves in the same way increasing from 7 to 17 for $n_L/n_G<0.35$ and then monotonously decreasing for higher densities reaching 4 at $n_L/n_G\simeq 0.7$. The same behavior is observed for the radial velocity fluctuations but with smaller variation between 5 and 10.

The behavior of the skewness and flatness factors confirm what can be deduced from the PDF plot. At normalized density ~0.35, the signals recorded in the far SOL are the most intermittent, suggesting that avaloids play their largest role in transport. Above and below the normalized density of 0.35, the signals tend to be more Gaussian and the role of avaloids decreases. One should keep in mind that this is true for the ion saturation current fluctuations but less true for the radial velocity fluctuations which seems to be less affected by the increase of the average density.

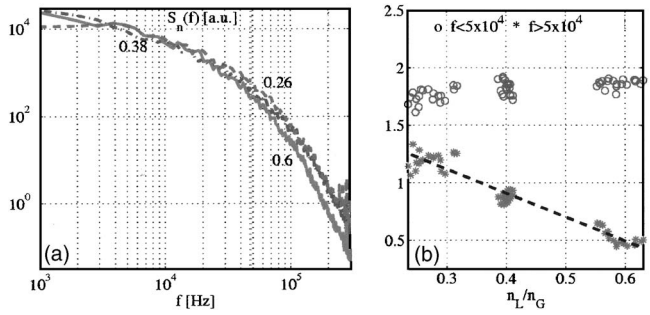

FIG. 5. In (a) is plotted in a log-log frame the power spectrum of the density fluctuations ($S_n(f)$) for normalized densities equal to 0.6 (solid line), 0.38 (dash-dotted line), and 0.26 (dashed line). The density fluctuations were normalized by their standard deviation. (b) shows the integration of the spectra for frequencies above (∗) and below (○) some critical frequency f_L=50 kHz. The position of f_L is shown in (a) by a thick dotted vertical line. Note that the high frequency contribution decreases with increasing n_L/n_G.

V. THE POWER SPECTRA AND THE BEHAVIOR OF SMALL AND LARGE SCALES WITH INCREASING NORMALIZED DENSITY

In this section, the power spectra are used in order to characterize the behavior of small and large scales as n_L/n_G is increased. The power spectrum is the Fourier transform of the auto-correlation function which was investigated in Ref. 28 for the Alcator C-MOD tokamak. The authors showed that the auto-correlation coefficient becomes larger as the density is increased. Here, we revisit the issue of auto-correlation but in the frequency domain in order to characterize the behavior of the various scales as a function of the normalized density. In this section, the Taylor's frozen turbulence hypothesis is assumed to hold where changes in time and space are assumed equivalent related by a global convection velocity.[38] Hence, one can associate high (small) frequencies to small (large) scales.

Figure 5(a) shows three power spectra taken at three normalized densities in a log-log frame. The signals that lead to these spectra were normalized by their standard deviation and their average value was set to 0. Consequently, it is the shape that is of interest here. One readily notices that the spectra change shape and that high and low frequency amplitudes do not behave in the same way with increasing n_L/n_G. The low frequency amplitudes appear to increase as a function of n_L/n_G; the opposite occurs for the high frequency amplitudes. In order to better emphasize this fact, we first noted that the change in the behavior of the different components of the spectrum takes place around $f_L\sim 50$ kHz. We then integrated the frequencies greater and smaller than f_L and plotted the result in Fig. 5(b). It was verified that the choice of f_L is not critical.

The high frequency component of the fluctuations decreases with increasing average density. This is interpreted as reflecting the decrease of the small scales' contribution. Later

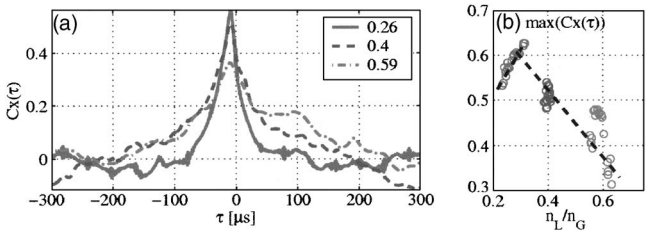

FIG. 6. (a) shows the cross-correlation coefficient between two poloidally separated tips biased to collect the ion saturation current. Three normalized densities are represented as 0.59 in dash-dotted line, 0.4 in dashed line, and 0.26 in solid line. The behavior of the cross-correlation amplitude is shown in more detail in (b) for a CDN configuration as a function of n_L/n_G.

in this article, it is shown that the radial velocity slightly increases by approximately ~10%. Hence, the effect of changing velocity while keeping f_L fixed can be neglected, and the changes in the spectra are not caused by the Doppler shift. The decrease of the small scales' fluctuations is caused by the increase of the various types of collisions that exist in the tokamaks SOL which damp the small scales of turbulence. Large scales' contribution on the other hand remains almost unchanged or slightly increases.

VI. THE POLOIDAL CROSS-CORRELATION PROPERTIES FUNCTION OF THE NORMALIZED DENSITY

Before moving on with the properties of avaloids independently of the background turbulence that represents diffusive type of transport, we discuss in this section the cross-correlation properties of the turbulent fluctuations. We make use of two poloidally separated tips, which are biased to the ion saturation current, to determine the cross-correlation properties as a function of the normalized density. The poloidal distance between the two probe tips is 2.13 cm.

The cross-correlation coefficient defined as

$$Cx(r) = \frac{\langle j_1(t) j_2(t+\tau)\rangle}{\sqrt{\langle j_1^2\rangle \langle j_2^2\rangle}}$$

is plotted in Fig. 6(a) for three different densities in the CDN configuration. The cross-correlation amplitude decreases with increasing n_L/n_G. With more details, this is depicted in Fig. 6(b). After a rise for low densities $n_L/n_G < 0.35$, the cross-correlation amplitude decreases monotonously from 0.63 to about 0.3. This indicates that there are fewer large scale structures with scales above 2.13 cm.

At the same time, the width of the cross-correlation coefficient increases with n_L/n_G. This enlargement can be caused by two phenomena. At constant velocity, this would be due to the increase of the turbulence macroscale. At a constant turbulence macroscale, this could be due to the decrease of the velocity. The poloidal velocity is deduced from the position of maximum cross-correlation. The distance between the two probes divided by the time shift yields the poloidal velocity. As one can deduce from Fig. 6(a), the time shift seems independent of the average velocity. Therefore, the increase in the width of Cx is mainly caused by that of the turbulent scales. The study of the radial and poloidal velocities and scales will be performed in more detail in the next section.

From this section, one can deduce that while the macroscale of turbulence, which includes both the diffusive and convective part, increases, the cross-correlation amplitude decreases. This reflects the fact that fewer large-scale structures exist with increasing n_L/n_G. This information is in agreement to the one deduced from the PDF where the amplitude of the bursts amplitude was observed to decrease.

VII. AVALOIDS PROPERTIES USING CONDITIONAL ANALYSIS

In the above three sections, we studied the signals using rather conventional methods such as the PDF and correlation functions. The results reflected the changes of the two components of transport that are convective and diffusive, as a function of the normalized density. In this section, conditional analysis is used to select the high intensity bursts on the ion saturation signals and investigate their properties independently of the background signal. The selection method was described several times.[30,31] It consists of normalizing j_{sat} and choosing the maxima that are greater than 2.5 the standard deviation. Once the selection process is done, one can determine the behavior with increasing normalized density of the auto-conditional average, the cross-condition averages, the time between bursts and the contribution of avaloids to the total radial transport. The investigation of each of these issues is detailed hereafter.

A. Auto- and cross-conditional averages

Let $N_{\max}$ be the number of maxima selected on an ion saturation signal with intensity greater than 2.5 the standard deviation. Around each maximum 50 points are selected to form a matrix of $N_{\max} \times 101$. The auto-conditional average (CA_{nn}) is obtained by averaging over the $N_{\max}$. The cross-conditional average is obtained by averaging over $N_{\max}$ of another signal that can be either another ion saturation current (CA_{n_1,n_2}), or a radial velocity (CA_{n,v_r}) or a radial turbulent flux (CA_{n,Γ_r}).

In Fig. 7(a) the auto-conditional average for three different normalized densities is plotted. The auto-conditional average represents a typical form of the bursts on the ion saturation current. As was noted, $CA_{n,n}$ is asymmetric in time reflecting the spatial shape of the burst as it is passes by the probe. It increases sharply at about -10 μs and decays rather slowly going back to 0 at about 50 μs. With increasing density, the amplitude of the bursts with respect to the standard deviation decreases. This is in agreement with the decrease of intermittency reported earlier using the PDF. The dependence of the maximum of $CA_{n,n}$ is shown in Fig. 8. After a short increase for normalized density below 0.35, the maxima of $CA_{n,n}$ decrease monotonously from five to three times the standard deviation. This takes place independently from the magnetic field configuration as the data plotted are recorded in LDN and CDN. As the amplitude decreases with increasing n_L/n_G, $CA_{n,n}$ width increases in agreement with the behavior of the cross-correlation coefficient.

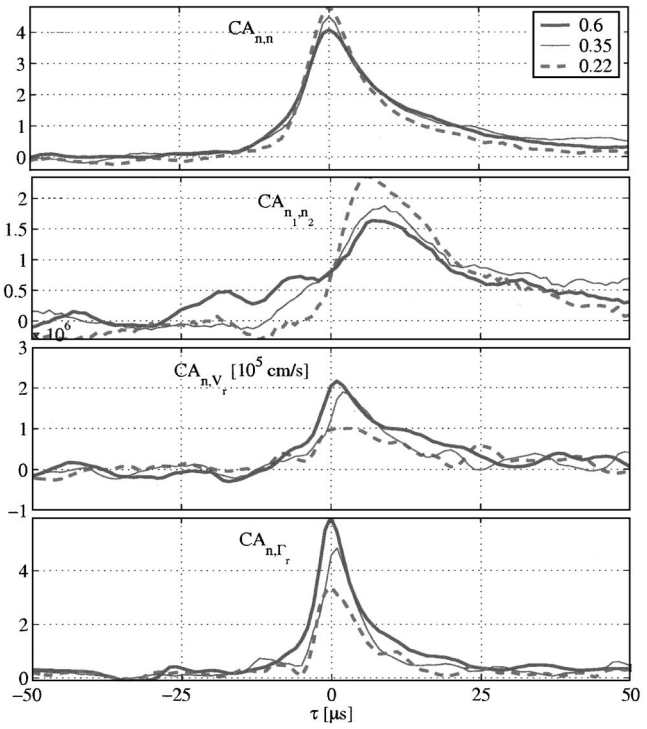

FIG. 7. The auto ($CA_{n,n}$) and cross-conditional average ($CA_{n_1,n_2}, CA_{n,V_r}, CA_{n,\Gamma_r}$) are plotted in (a), (b), (c), and (d). Three densities are represented as 0.22 by dashed line, 0.35 by solid line, and 0.6 by thick solid line. The density fluctuations were normalized by the standard deviation. The radial velocity is shown in km/s.

In Fig. 7(b) the cross-conditional average CA_{n_1,n_2} is shown, where maxima are selected on one probe and the average is taken on another probe that is poloidally separated by 2.31 cm. In comparison to $CA_{n,n}$, the amplitude drop is more important as it is a measurement that is more sensitive to the existence of large scale structures. In agreement with the behavior of $CA_{n,n}$, the width of the temporal profile of avaloids increases.

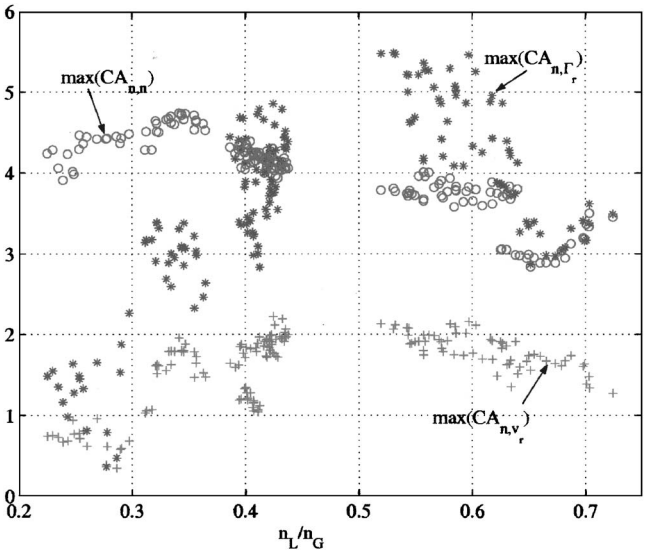

FIG. 8. The maxima of $CA_{n,n}$, CA_{n,V_r}, CA_{n,Γ_r} are plotted. With respect to the previous plot, the radial velocity and the flux are normalized by their standard deviation.

In Fig. 7(c), we plot the cross-conditional average of the radial $\vec{E}\times\vec{B}$ velocity determined from the two poloidally separated floating probes. Because v_r is not normalized, CA_{n,v_r} increases with increasing normalized density. The maxima of CA_{n,v_r} normalized to the standard deviation are plotted in Fig. 8. The radial velocity of avaloids increases with n_L/n_G until 0.35, then it decreases. The temporal shape of the cross-conditional average also increases in a consistent fashion with $CA_{n,n}$ and CA_{n_1,n_2}.

The turbulent flux is the product of the fluctuating density fluctuations deduced from j_{sat} and the fluctuating radial velocity is assumed to be dominated by the $\vec{E}\times\vec{B}$ term. The conditional average of the turbulent flux CA_{n,Γ_r} (non-normalized V_r) is plotted in Fig. 7(d). The amplitude of CA_{n,Γ_r} increases with increasing density reflecting. The behavior of $\max(CA_{n,\Gamma_r})$ normalized to the standard deviation of the radial turbulent flux with the normalized density is depicted in Fig. 8 where it increases for $n_L/n_G<0.35$ and then remains almost constant within the experimental precision.

In summary, the results obtained *via* conditional analysis confirms the existence of an intermediate critical normalized density where the properties of avaloids change. In agreement with the PDF results, the amplitude of the auto-conditional average normalized by the standard deviation decreases as n_L/n_G approaches unity. The amplitude of the radial flux after normalization, however, does not show the same decrease but appears to saturate.

B. Scaling with respect to the normalized density

As indicated earlier, the radial velocity is determined from two floating probe tips that are poloidally separated by 5 mm. The average radial velocity $\langle v_r\rangle=\langle E_\theta\rangle/B$ reflects that of avaloids and the background turbulence and may be determined by averaging over the poloidal electric field. The radial velocity of avaloids alone is obtained from the conditional averaging. The average poloidal velocity is determined using the cross-correlation coefficient (see Fig. 6) and the avaloids poloidal velocity is obtained using conditional averaging between the two ion saturation probe tips [Fig. 7(c)]. Hence, one can determine the behavior of avaloids and the overall signal, but far from the separatrix it is clear that avaloids dominate the signals properties. Consequently, we will focus on them alone.

In Fig. 9(a) the radial velocity deduced from cross-conditional averaging as a function of the normalized density is shown. Its behavior is similar to that of the standard deviation of the radial velocity shown in Fig. 4(c). On the average, the radial velocity increases for normalized densities smaller than 0.4 and then decreases when higher normalized densities are probed. The poloidal velocity of avaloids behave differently as it remains almost unchanged with increasing n_L/n_G.

Taking into account both the radial and poloidal velocities as well as the temporal width of the cross-conditional

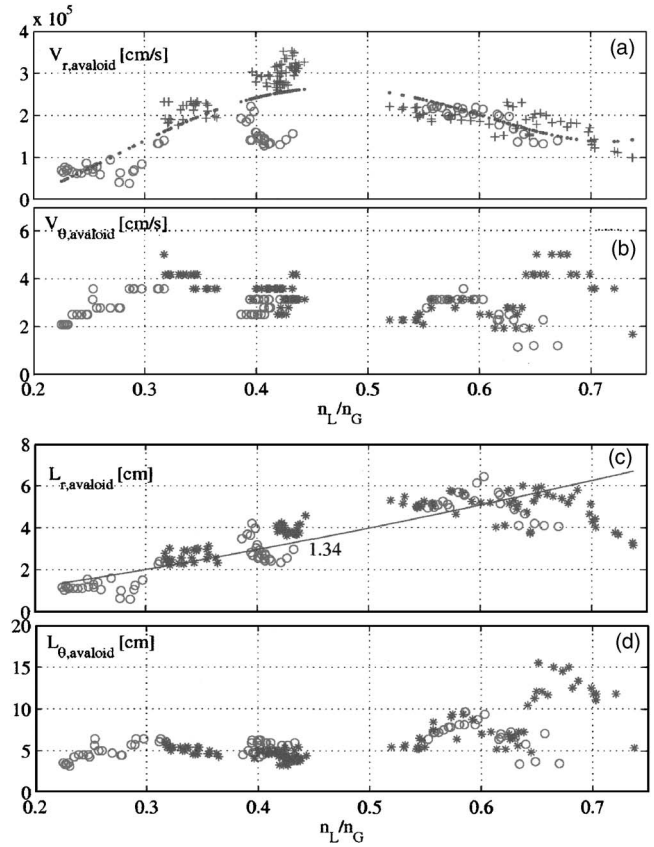

FIG. 9. (a) and (b) show, respectively, the radial and poloidal velocities of avaloids as a function of the normalized density [CDN (○) as well as LDN (∗) are used]. The same symbols are used in (c) and (d) where the radial and poloidal scales of avaloids are plotted as a function of the normalized density.

average, one can deduce the poloidal and radial length scales of avaloids. The result is plotted in Figs. 9(c) and 9(d) respectively. We obtain

$$L_{r,\text{avaloid}} \sim (n_L/n_G)^{1.34} \quad \text{and} \quad L_{\theta,\text{avaloids}} \sim (n_L/n_G)^0.$$

The radial scales of avaloids increase from approximately 1.6 to 6 cm. The increase of the radial length indicates that, as the average density increases, matter from regions that lie deeper into the closed field line regions is transported outside and vice versa due to vorticity. This is an interesting result showing that not only the turbulence level increases with normalized density but also the scales that couple different regions of the plasma. The increase is quite important suggesting stronger and faster coupling between the SOL and the plasma edge as the density is increased.

The poloidal scales, on the other hand, remain unchanged as the normalized density is increased. The poloidal length scale of avaloids is about 5 cm independently of the average value of the normalized density. The fact that the poloidal length scale is constant suggests that the mode number of the instability remains unchanged and this is what is investigated in the next section.

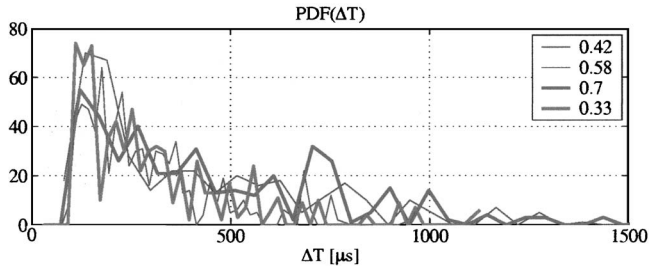

FIG. 10. The PDF of ΔT for four normalized densities with values shown in the figure legend. Within the error bars, the shape of the PDF is unchanged.

C. Statistics of the time between bursts

After selecting the maxima above 2.5 the standard deviation, ΔT is defined as the time between two bursts. Because it is the difference between two events, it is not affected by the Doppler shift and reflects the time between two avaloids to be ejected from the plasma. As a matter of fact, in linear devices it was shown that the time between bursts is related to oscillations inside the plasma.[32] Consequently, ΔT is an important quantity that reflects the frequency of the instability that generates avaloids.

In Fig. 10 five PDFs of ΔT for increasing normalized density are shown. The PDF displays a maximum at about 200 μs and an exponential decay for large separation times. It was shown that this feature is caused by intermittent detection rather than intermittent generation of avaloids.[32] Within the present experimental precision, the most probable frequency remains at about 5 kHz for all the normalized densities. It is thus deduced that the frequency of the instability giving rise to avaloids does not depend on the average density.

Low frequency instabilities that might lead to an oscillation at 5 kHz are excited by edge gradients. However, it is the scale length of these gradients that counts for the growth rate of these instabilities.[39] The present results can thus be interpreted as a consequence of the fact that gradient scale lengths at the plasma edge are little or not greatly modified by increasing the density (see also Ref. 23).

D. Avaloids contribution to the total radial turbulent flux

As indicated earlier, the radial turbulent velocity is determined using two poloidally separated floating tips. The density fluctuations are deduced from a probe biased to the ion saturation current. The average value of these two quantities is set equal to 0. Then, they are multiplied to form the turbulent radial flux $\Gamma_r(t)=n'(t)v_r'(t)$ where the primes denote fluctuations with average value equal to 0. In order to determine the contribution of avaloids to the total radial flux, we delete parts of the flux where high intensity bursts are found on the density fluctuations signal. The average yields the radial flux without the contribution of avaloids. The fluxes with and without avaloids are then averaged over time to yield Γ_r and $\Gamma_{r,\text{wa}}$, where the wa subscript means "without avaloids." The percentage of the contribution of avaloids with intensity above $2.5\sigma(j_{\text{sat}})$ is calculated as

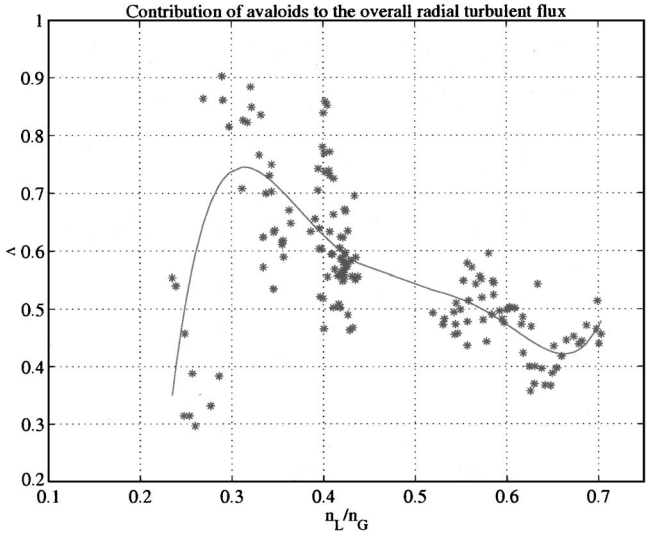

FIG. 11. The rate of contribution of avaloids to the overall turbulent radial transport (Λ) is shown as a function of the normalized density. Λ increases for normalized densities smaller than 0.35. For values greater than 0.35, Λ decreases.

$$\Lambda = \frac{\Gamma_r - \Gamma_{r,\mathrm{wa}}}{\Gamma_r}$$

and is plotted in Fig. 11.

The contribution of avaloids increases from 35% to approximately 75% in the range of normalized density below 0.35. After, the data clearly show a continuous decrease from 75% to 45% as the normalized density increases from 0.35 to 0.72. During this range, we recall that the rate of occupation of avaloids is almost constant. We deduce that the contribution of avaloids to the overall radial flux decreases with increasing density for normalized density values close to 1.

VIII. THE BEHAVIOR OF THE PLASMA AT THE TARGET PLATES

In order to have a comprehensive view of the SOL behavior as a function of the normalized density, it is necessary to investigate the behavior of the plasma at the target plates as all of the analyses above dealt with the midplane SOL. Earlier studies confirmed the role of field line expansion at the divertor targets and quantified the behavior of the temperature and density scale lengths.[40,41]

During the plasma discharge in MAST, the low-field strike points move outward away from the center stack. This comes from the fact that MAST solenoid is shorter than the vessel and close to the plasma due to the spherical tokamak (ST) geometry. In consequence, there is a large fringing field from the end of the solenoid. As the solenoid current ramps down during the shot, this fringing field changes and influences the divertor region field. As the strike point sweeps the divertor target plates, each probe records the variation around the strike point region. The ion saturation current density used here is situated around the outer-lower strike point. Consequently, they record the plasma behavior at the target plates in the private flux and the low-field regions. Data are recorded at a frequency of 1 MHz.

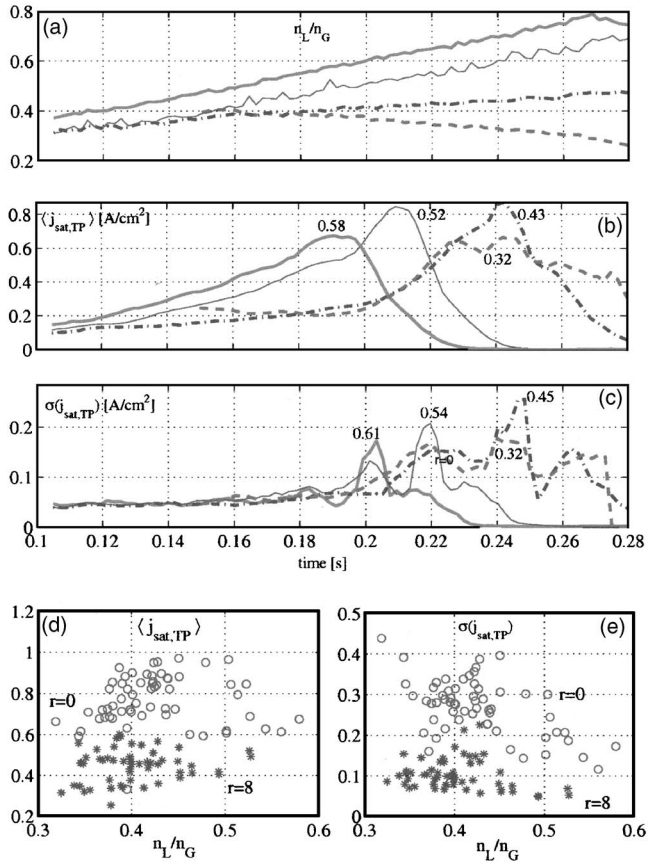

FIG. 12. (a) illustrates the average core density as a function of time for four plasma discharges (6843, 6844, 6847, and 6849). In (b) the average of $j_{sat,TP}$ as a function of time obtained on one of the target probes is shown. The rise and fall of the signal is caused by the motion of the strike point. On the left to the strike point lays the low-field SOL, on the right lays the private flux regions. In (c) the standard deviation as a function of time for the same discharges is shown. The numbers included represent the average normalized density value at maximum $\sigma(j_{sat})$. In (d) and (e) the average and standard deviation at $r=0$ (○) and $r=8$ cm (*) as a function of the normalized density are shown. Note that no increase of the different quantities is recorded as is the case at the midplane.

Because of the nonstationary character of the discharge where not only the density changes but also the strike points move, we decided to show in Fig. 12 the different quantities as a function of time. In Fig. 12(a) the normalized density as a function of time for the same four Ohmic L-mode discharges is plotted, where the plasma is in the lower LDN configuration. In Fig. 12(b) the average value of the ion saturation current density at the target probes is shown. The maxima denote the strike point; on its left is the low-field SOL and on its right the private flux region. The values of the normalized density at the strike point are illustrated in the graph so one can compare the different graphs. No increase is reported in any of the three regions of the average value as a function of the normalized density. This is also the case for the standard deviation plotted in Fig. 12(c). In order to show the evolution of the plasma at the target plates, we illustrate in Figs. 12(d) and 12(e), respectively, the behavior of the average and standard deviation of the ion saturation current density taken at the strike point and in the SOL at $r=8$ cm. No increase as the one reported at the midplane is observed

at the target for either of the two quantities. Accordingly, and in striking contradiction to what is happening at the midplane, the plasma at the targets in MAST does not know about the average density increase. It should be mentioned that the increase of the density at the midplane SOL occurs for all radii up to the separatrix. One can therefore deduce that even though the field lines connect the midplane to the target plates, this connection is inefficient. The main source of this decoupling between the two regions might be neutrals with a role that might have been enhanced by the distance between the X-point and the lower-outer strike point (low-field side). This distance is about 1 m larger than for C-MOD and other conventional tokamaks where it is only about 15 cm. In the case of C-MOD, and for normalized densities smaller than 0.4, a strong coupling is observed where the average and standard deviation of j_{sat} in the divertor region increase at the same rate as at the midplane.

We deduce that in MAST a decoupling exists between the midplane and the target region with respect to the average density in the plasma. Because the density limit is the same for MAST and C-MOD, this coupling to the target region does not seem to play an important role in setting the density limit.

IX. CONCLUSIONS

This article examined in details the properties of the SOL turbulence as a function of the average density in the MAST tokamaks. Several conclusions can be drawn from this work and are discussed below.

A. Critical normalized densities

According to the investigation of the role of avaloids and intermittency, there seems to be a critical value of the normalized density. The role of avaloids in overall turbulence peaks at $n_{cl} \sim 0.35$ and falls off at both lower and high normalized density. This is reflected in the skewness and flatness factors of the ion saturation current. They both show maximum deviation from the Gaussian values at n_{c1}.

For normalized densities that are greater than n_{c1}, intermittency decreases as the average density approaches n_G. This can be caused by two effects: the decrease of the intensity of bursts, and/or, the decrease of avaloids frequency. The probability distribution function of the time between events indicated that avaloids frequency is not changing with increasing density. This result is backed up by the fact that the poloidal length scale is independent of the average density. On the other hand, the decrease of the amplitude of high intensity bursts is obtained from the behavior of the auto-conditional average amplitude as it monotonously decreases for normalized density values greater than 0.35. As a consequence, the role of avaloids in the overall turbulent flux is observed to decrease from approximately 75% to 45% in this range.

B. Why avaloids role decreases

As noted the role of avaloids decreases with increasing density. Two main reasons lie behind this fact. First is that their frequency does not increase with the density. Second is the increase of the background turbulence level. It was shown in the PISCES linear device that avaloids in the far SOL are correlated to oscillation in the main plasma column.[32] Accordingly, avaloids frequency is set at the plasma edge. In order to change the frequency the gradients should change. However, this does not occur because turbulence also increases leading to approximately the same edge gradient. The second reason is avaloids relative intensity decrease. This is caused by the fact that avaloids live in a "turbulent" world on which their propagation paths, amplitudes, scales, and velocities depend. The more the background is turbulent, as it is with increasing average density, the more efficient is the mixing of avaloids with the background and thus the lesser are their amplitudes. At the same time, viscous damping at small scales increases leading to a net decrease of the high-frequency component of the fluctuations to the overall power.

TABLE I. Different properties of avaloids as a function of the normalized density.

$V_{r,\mathrm{avaloid}}$	increase and then saturates
$V_{\theta,\mathrm{avaloid}}$	$(n_L/n_G)^0$
$L_{r,\mathrm{avaloid}}$	$(n_L/n_G)^{1.34}$
$L_{\theta,\mathrm{avaloid}}$	$(n_L/n_G)^0$
$\langle \Delta T \rangle$	$(n_L/n_G)^0$
Λ (for $n_L/n_G > 0.35$)	$(n_L/n_G)^{-0.65}$

C. Scalings

In the Introduction, we mentioned that one of the goals of this article is to provide the scaling of avaloids properties with respect to the average density. This is a first step that is needed to be continued by scaling with respect to other parameters in order to have a reliable way to predict their role in future devices such as ITER. Table I summarizes the scalings obtained in this article.

D. The density limit

In conclusion, the density limit seems to be more affected by the diffusive turbulence rather than by avaloids. The main reason behind this fact is that turbulence destroys avaloids coherence by mixing them with the background. The higher the density is, the higher the turbulence is, the more is the mixing efficiency and the lesser avaloids play a role in the turbulent radial flux.

Another crucial aspect revealed by the present study is the increase of the radial scales of normal turbulence as well as avaloids. This means that, as the density is increased, plasma particles from regions that are more inside the last closed flux surface are radially transported outside the separatrix. Also it means that neutrals or/and cold plasma penetrates deeper inside the plasma edge. This is caused by eddies in the case of diffusive turbulence where vorticity transports hot plasma out and brings cold plasma in. The instability that causes avaloids also leads to a similar type of transport cold plasma inside the plasma via voids that are

caused by the crest of the oscillation. In consequence, we speculate that the plasma radiation could increase considerably, which could lead to an even larger decrease of the temperature, a pinching of the plasma current channel, and eventually to a global MHD disruptive instability. According to the above results and discussions, it is the whole region that is facing the low-field separatrix that plays the important role in setting the density limit. This might explain why the midplane coupling/decoupling to the target does not play an important role, and thus why different magnetic confinement devices with different designs of the target regions have the same density limit.

ACKNOWLEDGMENTS

Fruitful discussions with M. Greenwald and B. LaBombard are acknowledged.

This work was performed under the U.S. Department of Energy Contract No. DE-FG03-95ER-54301 and was jointly funded by Euratom and the UK Engineering and Physical Sciences Research Council.

[1] M. Murakami, J. D. Callen, and L. A. Berry, Nucl. Fusion **16**, 347 (1976).
[2] P. E. Stott, J. Hugill, and S. J. Fielding, in *Proceedings of the 8th European Conference Prague* (PUBLISHER, Geneva, Switzerland, 1977), Vol. 1, p. 37.
[3] M. Greenwald *et al.*, Nucl. Fusion **28**, 2199 (1988).
[4] T. W. Petrie, A. G. Kellman, and A. A. Mahdavi, Nucl. Fusion **33**, 929 (1993).
[5] B. LaBombard, J. A. Goetz, C. Kurz *et al.*, Phys. Plasmas **2**, 2242 (1995).
[6] O. Gruber, V. Mertens, J. Neuhauser *et al.*, Plasma Phys. Controlled Fusion **39**, B19 (1997).
[7] R. Maingi, M. A. Mahdavi, T. C. Jernigan *et al.*, Phys. Plasmas **4**, 1752 (1997).
[8] J. Rapp, P. C. de Vries, F. C. Schuller *et al.*, Nucl. Fusion **39**, 765 (1999).
[9] L. Giannone, J. Baldzhun, R. Burhenn *et al.*, Plasma Phys. Controlled Fusion **42**, 603 (2000).
[10] M. Greenwald, Plasma Phys. Controlled Fusion **44**, R27 (2002).
[11] D. L. Brower, C. X. Yu, and R. V. Bravenec, Phys. Rev. Lett. **67**, 200 (1991).
[12] M. M. Marinak, Nucl. Fusion **35**, 399 (1995).
[13] B. Unterberg, A. Messiaen, J. Ongena, and M. Brix, Plasma Phys. Controlled Fusion **39**, B189 (1997).
[14] E. Minardi, Plasma Phys. Controlled Fusion **26**, 1505 (1984).
[15] F. A. Haas and A. Thyagarja, Plasma Phys. Controlled Fusion **28**, 1093 (1986).
[16] K. Borrass, D. J. Campbell, S. Clement, and G. C. Vlases, Nucl. Fusion **33**, 63 (1993).
[17] A. V. Chankin, Plasma Phys. Controlled Fusion **39**, 1059 (1997).
[18] J. W. Connor and S. You, Plasma Phys. Controlled Fusion **44**, 121 (2002).
[19] M. V. Umansky, S. I. Krasheninnikov, B. LaBombard, and J. L. Terry, Phys. Plasmas **5**, 3373 (1998).
[20] S. K. Erents, J. A. Tagle, and G. M. McCrakcken, J. Nucl. Mater. **162–164**, 226 (1989).
[21] B. LaBombard, M. V. Umansky, and R. L. Boivin, Nucl. Fusion **40**, 2041 (2000).
[22] B. LaBombard, R. L. Boivin, and M. Greenwald, Phys. Plasmas **8**, 2107 (2001).
[23] B. Lipschultz, B. LaBombard, C. S. Pitcher, and R. Boivin, Plasma Phys. Controlled Fusion **44**, 733 (2002).
[24] S. J. Zweben and R. W. Gould, Nucl. Fusion **25**, 171 (1983).
[25] R. Jha, P. K. Kaw, and S. K. Mattoo, Phys. Rev. Lett. **69**, 1375 (1992).
[26] M. Endler *et al.*, Nucl. Fusion **35**, 1307 (1995).
[27] R. A. Moyer, R. D. Lehmer, and T. E. Evans, Plasma Phys. Controlled Fusion **38**, 1273 (1996).
[28] B. A. Carreras, V. E. Lynch, and B. LaBombard, Phys. Plasmas **8**, 3702 (2001).
[29] G. Antar, P. Devynck, X. Garbet, and S. C. Luckhardt, Phys. Plasmas **8**, 1612 (2001).
[30] G. Y. Antar, S. I. Krasheninnikov, and P. Devynck, Phys. Rev. Lett. **87**, 065001 (2001).
[31] G. Antar, G. Counsell, and Y. Yu, Phys. Plasmas **10**, 419 (2003).
[32] G. Antar, Phys. Plasmas **10**, 3629 (2003).
[33] ITER Physics Basis, Nucl. Fusion 39 (1999).
[34] A. Sykes, J.-W. Ahn, and R. Akers, Phys. Plasmas **8**, 2101 (2001).
[35] A. Kirk, G. F. Counsell, and E. Arends, Plasma Phys. Controlled Fusion **46**, A187 (2004).
[36] G. F. Counsell, A. Kirk, and J.-W. Ahn, Plasma Phys. Controlled Fusion **44**, 827 (2002).
[37] H. Meyer, A. R. Field, and R. J. Akers, Plasma Phys. Controlled Fusion **46**, A291 (2004).
[38] A. S. Monin and A. M. Yaglom, *Statistical Fluid Mechanics* (MIT Pess, Cambridge, MA, 1971).
[39] F. F. Chen, *Plasma Physics and Controlled Fusion* (Plenum, New York, 1984).
[40] J.-W. Ahn and G. F. Counsell, J. Nucl. Mater. **290–293**, 820 (2001).
[41] G. Y. Antar *et al.*, Phys. Plasmas **12**, 032506 (2005).